2-28-2003

A Modeling Study of O2 and OH Airglow Perturbations Induced by Atmospheric Gravity Waves

Alan Z. Liu
Embry Riddle Aeronautical University - Daytona Beach, liuz2@erau.edu

Gary R. Swenson
University of Illinois at Urbana-Champaign

JOURNAL OF GEOPHYSICAL RESEARCH, VOL. 108, NO. D4, 4151, doi:10.1029/2002JD002474, 2003

A modeling study of O_2 and OH airglow perturbations induced by atmospheric gravity waves

Alan Z. Liu and Gary R. Swenson

Department of Electrical and Computer Engineering, University of Illinois at Urbana-Champaign, Urbana, Illinois, USA

Received 23 April 2002; revised 4 October 2002; accepted 6 December 2002; published 28 February 2003.

[1] A one-dimensional model is used to investigate the relations between gravity waves and O_2 and OH airglows perturbations. The amplitude and phase of the airglow perturbations induced by gravity waves (with period > 20 min) are calculated for different vertical wavelength (10–50 km) and damping rate. The model shows that for vertically propagating gravity waves, the amplitude of airglow perturbations observed from ground is larger for longer vertical wavelength, because of the smaller cancellation effect within each layer. The ratio of the amplitudes between O_2 and OH is smaller for larger wave damping. For upward propagating (downward phase progression) waves, the intensity perturbation in O_2 leads OH, and their phase difference (O_2 minus OH) is larger for smaller vertical length and/or stronger damping. The rotational temperature perturbation leads intensity perturbation in both layers. Their phase difference is also larger for smaller vertical length but is smaller for stronger damping. Based on these relations, the vertical wavelength and damping rate of gravity waves can be derived from simultaneous measurements of airglow perturbations in O_2 and OH layers. *INDEX TERMS:* 0310 Atmospheric Composition and Structure: Airglow and aurora; 0341 Atmospheric Composition and Structure: Middle atmosphere—constituent transport and chemistry (3334); 0394 Atmospheric Composition and Structure: Instruments and techniques; 3334 Meteorology and Atmospheric Dynamics: Middle atmosphere dynamics (0341, 0342); 3384 Meteorology and Atmospheric Dynamics: Waves and tides; *KEYWORDS:* gravity waves, airglow, wave dissipation, mesopause region

Citation: Liu, A. Z., and G. R. Swenson, A modeling study of O_2 and OH airglow perturbations induced by atmospheric gravity waves, *J. Geophys. Res.*, *108*(D4), 4151, doi:10.1029/2002JD002474, 2003.

1. Introduction

[2] The effects of atmospheric gravity waves (AGWs) are important factors in the momentum and thermal balance in the middle atmosphere. One major consideration in the studies of wave effects in the mesosphere is to discern their vertical propagation characteristics, i.e., whether they are vertically propagating or are ducted, reflected or breaking. *Walterscheid et al.* [1999, 2000] have analyzed a number of cases of relatively long period AGWs where ducting and/or reflection of waves is evident. When waves become evanescent, they have no vertical propagation hence no vertical momentum flux. Ducted waves consist of both upward and downward propagating waves, whose momentum fluxes cancel each other. It is therefore important to distinguish these waves to correctly estimate the momentum flux. The net effect of AGWs on the momentum balance depends on the divergence of their momentum flux. The momentum flux would have no effect on the background atmosphere if there is no wave dissipation or breaking. Determining the magnitude of wave dissipation is therefore equally important to assess the AGW effect. Airglow measurements have been widely used to study AGWs in the middle atmosphere [e.g., *Viereck and Deehr*, 1989; *Zhang et al.*, 1993a; *Reisin and Scheer*, 1996; *Walterscheid et al.*, 1999; *Hecht et al.*, 2001b]. Theoretical and modeling studies have greatly enhanced the understanding of the relation between the airglow perturbation and AGWs (*Walterscheid et al.* [1987], *Schubert and Walterscheid* [1988], *Tarasick and Shepherd* [1992a, 1992b], *Hickey et al.* [1993], *Zhang et al.* [1993a, 1993b], *Makhlouf et al.* [1995], among others). The perturbations generated by AGWs can be observed in both airglow intensity and the rotational temperature measurements. Their relation is a complex function of wave parameters often described by the Krassovsky parameter η [*Krassovsky*, 1972; *Walterscheid et al.*, 1987]. Because the airglow observed from ground is an integral effect of the entire airglow layer, some important wave parameters, such as the vertical wavelength and vertical propagation direction cannot be determined directly in a single layer observation. They can only be inferred based on theoretical prediction [e.g., *Reisin and Scheer*, 1996].

[3] Simultaneous observations of multiple airglow layers at various altitudes can provide much more information about AGWs. The vertical wavelength and propagation direction can be derived from the phase information of perturbation observed in multiple layers, and used to verify against theoretical predictions based on single layer observation. Wave dissipation rate can also be estimated by

0148-0227/03/2002JD002474$09.00

comparing the amplitudes of wave perturbation among several layers. For example, *Reisin and Scheer* [1996] compared the amplitude ratio in O_2 and OH layers with simultaneous O_2 and OH measurements, and *Ejiri et al.* [2001] identified a downward propagating wave with simultaneous observation of four airglow layers.

[4] Most modeling studies of airglow response to AGWs focused on a single layer, such as OH [*Tarasick and Shepherd*, 1992b; *Makhlouf et al.*, 1995], O_2 [*Tarasick and Shepherd*, 1992a; *Hickey et al.*, 1993; *Zhang et al.*, 1993b] and O(^1S) [*Hickey et al.*, 1997]. In this study, we use a one-dimensional model to examine the relation between AGWs and airglow perturbations in two commonly observed airglow layers, the O_2 Atmospheric band and the OH Meinel band. By modeling these two layers together, the phase and amplitude relation between these two airglows can be examined. The objective is to understand the mechanisms that cause the phase and amplitude differences between these two layers as perturbed by a single AGW. The relations between the intensity and rotational temperature perturbations in the two airglow layers provide wave information, including vertical wavelength and dissipation rate.

2. Model Description

2.1. Airglow Photochemistry

[5] For the O_2 Atmospheric band, the chemical reactions involved in the emission can be described as a two-step process (the Barth mechanism):

$$O + O + M(O_2 + N_2) \rightarrow O_2\left(c^1\Sigma_u^-\right) + M, \tag{1}$$

$$O_2\left(c^1\Sigma_u^-\right) + O_2 \rightarrow O_2\left(b^1\Sigma_g^+\right) + O_2, \tag{2}$$

[*Solheim and Llewellyn*, 1979; *Greer et al.*, 1981; *Torr et al.*, 1985; *Murtagh et al.*, 1990]. The volume emission rate for this process can be expressed as

$$\varepsilon_{O_2} = \frac{k_1 A_1 [O]^2 ([O_2] + [N_2])[O_2]}{\left(A_2 + K_2^{O_2}[O_2] + K_2^{N_2}[N_2]\right)(7.5[O_2] + 33[O])} \tag{3}$$

[*Murtagh et al.*, 1990; *McDade et al.*, 1986; *Zhang et al.*, 1993b], where $k_1 = 4.7 \times 10^{-33}\ (300/T)^2\ cm^6 s^{-1}$ is the rate coefficient for three-body recombination of O, $A_1 = 0.079\ s^{-1}$, the (0-0) band transition probability, $A_2 = 0.083\ s^{-1}$, the inverse radiative lifetime of O_2 ($b^1\Sigma_g^+$), $K_2^{O_2} = 4.0 \times 10^{-17}$ $cm^3 s^{-1}$ and $K_2^{N_2} = 2.2 \times 10^{-15}\ cm^3 s^{-1}$, the rate coefficients for quenching of O_2 ($b^1\Sigma_g^+$) by O_2 and N_2, respectively.

[6] The OH Meinel emission is described by,

$$H + O_3 \xrightarrow{k_4} OH^* + O_2, \tag{4}$$

and the volume emission rate is

$$\varepsilon_{OH} = \frac{f_8 [O][O_2]\left(k_6^{N_2}[N_2] + k_6^{O_2}[O_2]\right)}{(260 + 2 \times 10^{-11}[O_2])}, \tag{5}$$

where $f_8 = 0.29$ is fraction of emission at level 8, $k_6^{N_2} = 5.7 \times 10^{-34}\ (300/T)^{2.62}$ and $k_6^{O_2} = 5.96 \times 10^{-34}\ (300/T)^{2.37}$ are quenching coefficients. The brackets [ ] represent number densities in unit of cm^{-3}. ε_{O_2} and ε_{OH} are in unit of photons $cm^{-3}\ s^{-1}$.

2.2. Wave Perturbations

[7] Following conventional assumption, we consider an isothermal, windless atmosphere. A wave perturbation in temperature T' and density ρ' can be written as

$$(T'/T_u, \rho'/\rho_u) = \Re\left\{(\hat{T}, \hat{\rho}) e^{\alpha z + i(kx + ly + mz - \omega t)}\right\}, \tag{6}$$

where T_u and ρ_u are the unperturbed values, $\hat{T}$ and $\hat{\rho}$ the complex amplitudes, ω the intrinsic frequency, k and l the horizontal wavenumbers in x and y directions, respectively. The vertical structure of the perturbation is represented by the vertical wavenumber m and the exponential component α. Mathematically, m and α are respectively the real and imaginary parts of the eigen value in the vertical dimension. The parameters ω, k, l, m and α are all real numbers. Their relation is specified by the wave dispersion relation. There are two types of AGWs [*Hines*, 1960]. The first type of AGW is the vertically-propagating wave (the internal AGW) that satisfies the following dispersion relation [*Zhang et al.*, 1993b],

$$m^2 = \frac{\omega_b^2 - \omega^2}{\omega^2 - f^2} k_h^2 + \frac{\omega^2}{\gamma g H} - \frac{1}{4H^2}, \tag{7}$$

$$\alpha = \frac{1}{2H}, \tag{8}$$

where $k_h = \sqrt{k^2 + l^2}$ is the horizontal wavenumber, ω_b the Brunt-Vaisala (buoyancy) frequency, f the inertial frequency, γ the ratio of specific heats, H the scale height, and g the gravitational acceleration. Without dissipation, the wave amplitude grows exponentially with e-folding distance of $2H$ as indicated by (8). For this type of waves, the relation between the temperature and density perturbation is [*Walterscheid et al.*, 1987]

$$\hat{\rho} = \frac{1 - 2\omega^2 H/[g(\gamma - 1)] - 2iHm}{1 - 2\omega^2 H/g + 2iHm} \hat{T}. \tag{9}$$

Since the coefficient is complex, the phase difference between T' and ρ', i.e., the phase of T' minus the phase of ρ', varies with ω and m. Figure 1 shows this phase difference for various λ_z. For small λ_z and short period, ρ' and T' is nearly 180° out of phase. For wave period >20 min, there is little change in the phase difference between T' and ρ'. For wave period <10 min, the phase difference changes quickly, especially for waves with large λ_z.

[8] The second type of AGW is the evanescent wave which satisfies [*Zhang et al.*, 1993b]

$$m = 0, \tag{10}$$

$$\alpha = \frac{1}{2H} \pm \sqrt{\frac{1}{4H^2} - \frac{\omega^2}{\gamma g H} - \frac{\omega_b^2 - \omega^2}{\omega^2 - f^2} k_h^2}. \tag{11}$$

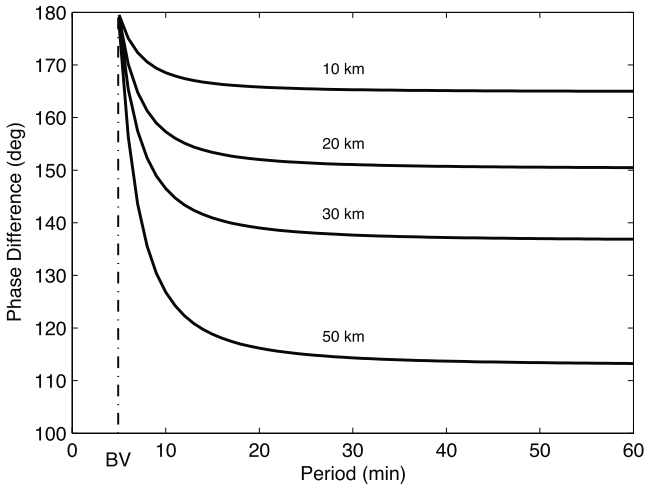

Figure 1. Phase differences between T' and ρ' (phase of T' minus phase of ρ') for λ_z = 10, 20, 30 and 50 km, as functions of wave period.

This type of waves does not have vertical propagation, but its amplitude increases exponentially with altitude in the absence of dissipation. The phase relation between the temperature and density for this type of waves is [*Walterscheid et al.*, 1987]

$$\hat{\rho} = \frac{1 - \alpha H - \omega^2 H/[g(\gamma - 1)]}{\alpha H - \omega^2 H/g}\hat{T}, \tag{12}$$

where α is determined by (11). Because the coefficient is real, T' and ρ' are either in phase or out of phase.

[9] Following (6), the temperature perturbation in the model is specified in the following form,

$$T'(z) = T_u(z)\Re\left\{\hat{T}e^{(1-\beta)z/(2H)+i(mz-\omega t)}\right\}, \tag{13}$$

for vertically propagating waves. Here the horizontal component $kx + ly$ is omitted since the model is one-dimensional and x and y can be arbitrarily set to zero. Note that the horizontal wavenumber k_h is not zero and can be calculated from (7) for vertically propagating waves once ω, m and other parameters are known. A damping factor β is introduced to simulate the effect of wave dissipation. β = 0 represents no dissipation; β = 1 represents saturated waves whose amplitude does not change with altitude; and $\beta > 1$ represents large dissipation with the wave amplitude decreasing with altitude. We use a constant damping rate throughout the altitude range for simplicity. In the real atmosphere, the wave dissipation rate is not a constant. β can be considered as the average dissipation rate between the OH and O_2 layers, which are separated by about 5 km.

[10] Given T', ρ' can then be determined from (9) or (12). The perturbation of number densities for major gases are simply,

$$\frac{[N_2]'}{[N_2]_u} = \frac{[O_2]'}{[O_2]_u} = \frac{\rho'}{\rho_u}, \tag{14}$$

and the atomic oxygen density perturbation is [*Walterscheid et al.*, 1987; *Zhang et al.*, 1993b]

$$\frac{[O]'}{[O]_u} = -DH\frac{\rho'}{\rho_u} + \frac{1 + DH}{\gamma - 1}\frac{T'}{T}, \tag{15}$$

where $D = d\ln [O]_u/dz$ is the inverse of the local scale height of unperturbed [O]. The volume emission rates are then calculated with (3) and (5).

[11] In ground-based observations the airglow intensity and the rotational temperature are two commonly measured quantities. The airglow intensity I is the vertical integral of the volume emission rate, and the rotational temperature T_R is the vertical integral of the air temperature weighted by the profile of the volume emission rate, with the assumption that the airglow molecules are in thermal equilibrium with the atmosphere. They are defined as

$$I(t) = \int_{z_1}^{z_2} \varepsilon(z,t)dz, \tag{16}$$

$$T_R(t) = \frac{1}{I(t)}\int_{z_1}^{z_2} \varepsilon(z,t)T(z,t)dz, \tag{17}$$

where T is the air temperature. Their perturbations are

$$I'(t) = I(t) - \langle I(t)\rangle, \tag{18}$$

$$T_R'(t) = T_R(t) - \langle T_R(t)\rangle, \tag{19}$$

where the brackets represent time mean. For a single sinusoidal wave, $I'(t)$ and $T_R'(t)$ are sinusoidal functions of time, so their amplitudes and phases can be easily determined from the time series. The dependencies of amplitude and phase of I' and T_R' on wave parameters can then be calculated.

[12] The unperturbed temperature, atmospheric density and number densities of various constituents are obtained from MSIS90 model [*Hedin*, 1991] at 35°N for spring equinox condition. The unperturbed temperature, $[O_2]$, $[N_2]$ and [O] profiles are shown in Figure 2. Both $[O_2]$ and $[N_2]$ decreases exponentially with altitude. Atomic oxygen density increases with altitude below 98 km and decreases gradually above. The corresponding unperturbed O_2 and OH emission profiles are shown as thick solid lines in Figure 3. The centroid height of the unperturbed O_2 emission is 94.7 km with full-width-half-maximum (FWHM) of 9.2 km. It is consistent with observation by *Burrage et al.* [1994]. The centroid height of the unperturbed OH emission is 89.5 km with FWHM of 11.1 km. The O_2 layer is therefore about 5 km higher than OH layer and is about 2 km thinner. These characteristics are listed in Table 1.

[13] For the results shown here, we choose a wave period of 2 hr. The results also apply to any waves with period longer than 20 min as indicated in Figure 1. The scale height H = 6 km. The vertical integration is between z_1 = 75 km and z_2 = 110 km, which covers the entire O_2 and OH emission

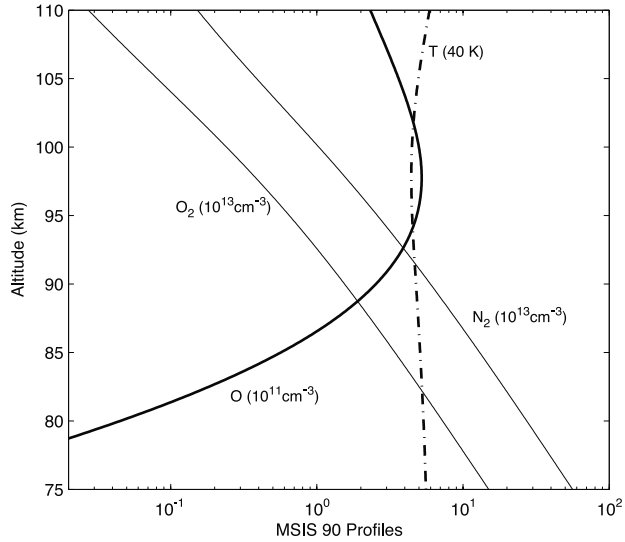

Figure 2. Temperature and number density profiles of O_2, N_2 and O based on MSIS90. They are used as unperturbed state in the model.

layers. $f = 8.365 \times 10^{-5}$ s^{-1} is the inertial frequency at 35°N, corresponding to an inertial period of about 21 hr. The effect of f is negligible when the wave period is within a few hours.

3. Model Results

[14] The objective of the model calculation is to obtain the relations between the observable quantities I' and T'_R and the two waves parameters λ_z and β. In the next subsection,we first study one particular set of the parameters (λ_z = 25 km and β = 1) to understand the relation between AGW perturbation and I' and T'_R. In subsection 3.2, we focus on the effects of λ_z with a fixed value of β = 1, which represents saturated waves. The amplitude of a saturated wave does not change with altitude, which makes it easier to identify and understand other factors that influence the amplitude and phase of I' and T'_R. Saturated waves are also commonly observed in the mesopause region. In subsection 3.3, we introduce additional variation in β to examine its effects on the amplitude and phase of I' and T'_R. β is varied from 0 for freely-propagating waves to 3 for heavily damped waves.

Table 1. Centroid Heights and Thicknesses (Measured by FWHM) of Unperturbed Volume Emission Profiles and Profiles of Standard Deviation of Volume Emissions Perturbed by a Saturated, Vertically Propagating Gravity Wave (β = 1 and λ_z = 25 km) for O_2 and OH

	Centroid Height	FWHM
unperturbed	94.7 km	9.1 km
unperturbed ε_{OH}	89.5 km	11.1 km
std(perturbed ε_{O_2})	92.0 km	7.5 km
std(perturbed ε_{OH})	86.4 km	9.1 km

3.1. A Typical Wave Perturbation

[15] The model response to a hypothetical, but typical wave is helpful for perspective and insight into the volume emission layer distortion associated with wave propagation through the respective layer. Figure 3 shows the profiles of unperturbed and perturbed OH and O_2 volume emission

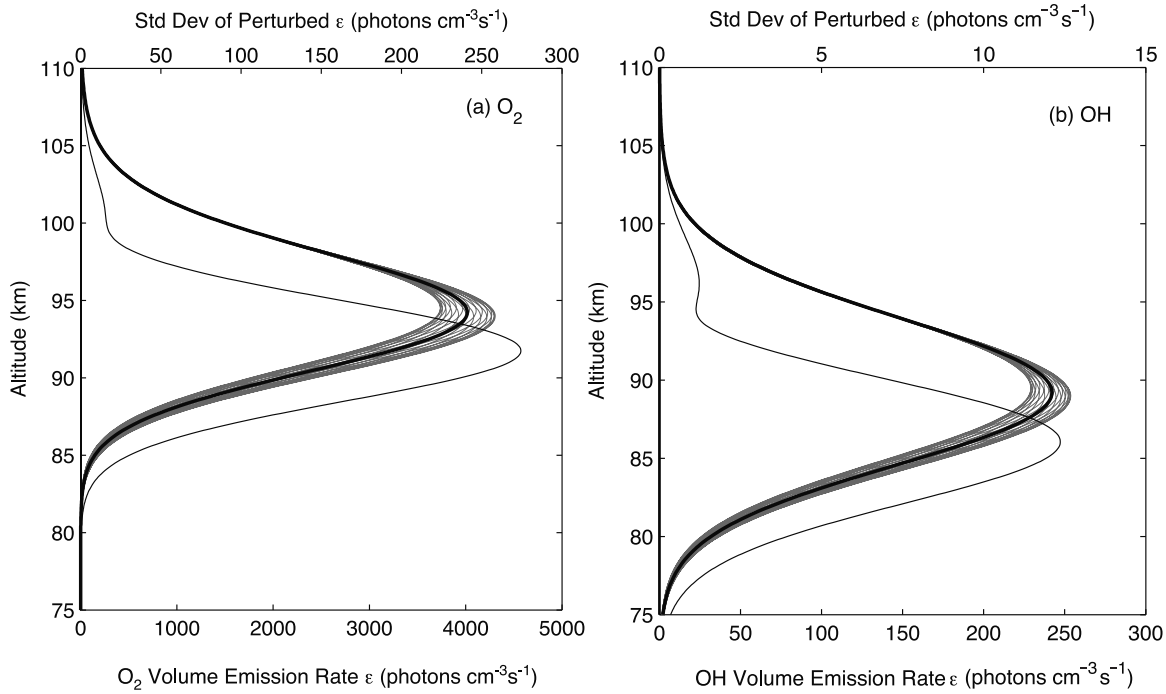

Figure 3. Unperturbed (thick solid line) and perturbed (thin gray lines) (a) O_2 and (b) OH volume emission rates, generated by a gravity wave perturbation with 2% amplitude in temperature. The wave amplitude does not change with altitude (β = 1) and λ_z is 25 km. The gray lines represent waves at 24 different phases, each 15° apart. These lines use the bottom axis. The thin solid line is the standard deviation of the perturbed emission with respect to the unperturbed one, using the upper axis.

rates, as the result of an upward propagating (downward phase progression) wave with λ_z = 25 km. Each gray line represents the perturbed emission at one phase, and all 24 lines cover the entire period with 15° phase increment. This figure gives a typical picture of the OH and the O_2 volume emission profiles perturbed by an AGW. An important feature is that the perturbations are not symmetric with respect to the altitude of the maximum unperturbed emission. The wave generates larger perturbations in the lower part of the emission layer than in the upper part. This is clearly shown by the profiles of the standard deviation of the perturbed emission (thin solid lines) with respect to the unperturbed emission. The centroid heights of these two profiles are 92.0 km and 86.4 km, which are 2.7 km and 3.1 km lower than the centroid heights of the unperturbed O_2 and OH emissions, respectively (Table 1). The mechanism for this asymmetry is discussed by *Swenson and Gardner* [1998] for the OH layer and is similar for the O_2 layer.

[16] These characteristics have several consequences to the I' and T'_R observed from ground. First, I' and T'_R are only sensitive to perturbations by waves with λ_z of about 10 km or longer, because shorter waves have strong cancellation inside the emission layer so they cannot be easily detected. The OH layer is thicker than the O_2 layer, which suggests that for small λ_z waves, the cancellation effect would be larger in OH layer than in O_2 layer. Secondly, if a wave propagates through both OH and O_2 layers, there would be a phase difference between the intensity perturbations I'_{OH} and I'_{O_2} because of the vertical separation (about 6 km) between these two layers. Thirdly, since the altitude of the maximum perturbation of volume emission is lower than the altitude of the peak volume emission, and T_R is the temperature weighted by the volume emission profile, the effective altitudes of the observed I' and T'_R are different. Hence there is also a phase difference between I' and T'_R in each layer for vertically propagating AGWs.

3.2. Effects of λ_z on Amplitude and Phase for Saturated Waves

3.2.1. Amplitude

[17] The observed amplitudes of I' and T'_R largely depend on the vertical wavelength of the waves. Because of the thickness of the emission layers, airglow and temperature perturbations induced by waves with small λ_z would have a strong cancellation effect and consequently a smaller amplitude in I' and T'_R. This cancellation effect can be measured by the ratio of the amplitude of I' or T'_R to the amplitude of the perturbing AGW. A Cancellation Factor (CF) can thus be defined for the airglow intensity as

$$\mathrm{CF}_I = \frac{\max(I'/\langle I\rangle)}{\max\left(T'_w/\langle T_w\rangle\right)}, \tag{20}$$

where T_w and T'_w are the temperature and temperature perturbation at a reference altitude. Note that they are the atmospheric temperature at a certain altitude, different from the rotational temperature defined in (17). Similarly, CF for T_R is defined as

$$\mathrm{CF}_{T_R} = \frac{\max\left(T'_R/\langle T_R\rangle\right)}{\max\left(T'_w/\langle T_w\rangle\right)}. \tag{21}$$

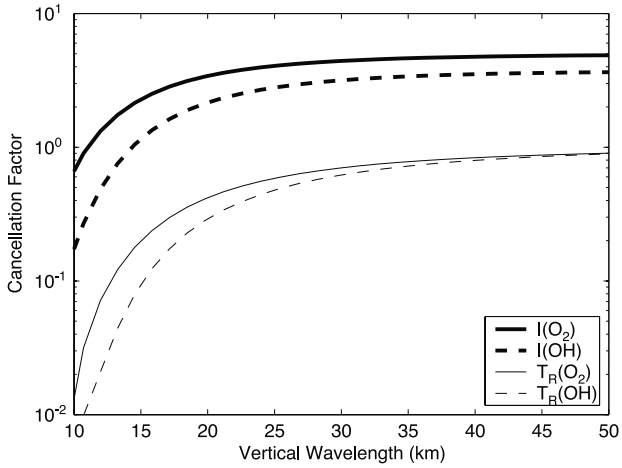

Figure 4. Cancellation factors of I' (thick lines) and T'_R (thin lines) for O_2 (solid lines) and OH (dashed lines), for waves with a period of 2 hr and the amplitude being constant with altitude (β = 1).

With this definition, smaller CF represents stronger cancellation.

[18] Figure 4 shows the CFs in both layers as functions of λ_z for upward propagating, saturated (β = 1) waves. It shows that for both O_2 and OH emissions, the CFs of I' and T'_R increase monotonically with increasing λ_z. For small λ_z, the CFs decrease sharply as the cancellation effect becomes strong. The airglow is therefore not sensitive to waves with λ_z < 10 km. The CFs for O_2 are larger than OH, indicating that the O_2 airglow is more sensitive to AGWs. This is mainly because the O_2 emission is roughly proportional to $[O]^2$ (equation (3)) while the OH emission is proportional to [O] (equation (5)). As $\lambda_z \to \infty$, the layer thickness becomes irrelevant, so the CF of T'_R approaches one. We also note that CFs for I' is larger than CFs for T'_R in both layers, with a gain factor of over 3 for the long waves. This shows that I' is more sensitive to AGW than T'_R.

[19] Figure 5a shows the ratios of relative amplitudes of I' to T'_R in the O_2 and the OH layers. They are the amplitudes of Krassovsky parameter η. Their values vary between 4 and 10 for λ_z > 15 km, comparable with other modeling [*Zhang et al.*, 1993b] and observational [*Reisin and Scheer*, 1996] studies. Figure 5b shows the ratios of relative amplitudes of I'_{O_2} to I'_{OH} and T'_{R,O_2} to $T'_{R,OH}$. These ratios are mainly determined by the growth rate of AGWs as they propagate through the two layers. For the damping rate β = 1, the wave amplitude does not change with altitude. The differences of the relative amplitudes of I' and T'_R between these two layers are therefore only due to the difference in dynamical and chemical response to AGWs. The amplitude ratio of I' varies from 2 to 1.3 as λ_z increases from 15 km to 50 km. The amplitude ratio of T'_R approaches 1 as λ_z increases (Figure 5b). The larger O_2 to OH ratios for smaller λ_z in both I' and T'_R is related to the difference in layer thickness of O_2 and OH as discussed above. As shown in Table 1 and Figure 3, the FWHM of the OH layer is larger than that of the O_2 layer, which results in a stronger cancellation effect in the OH layer.

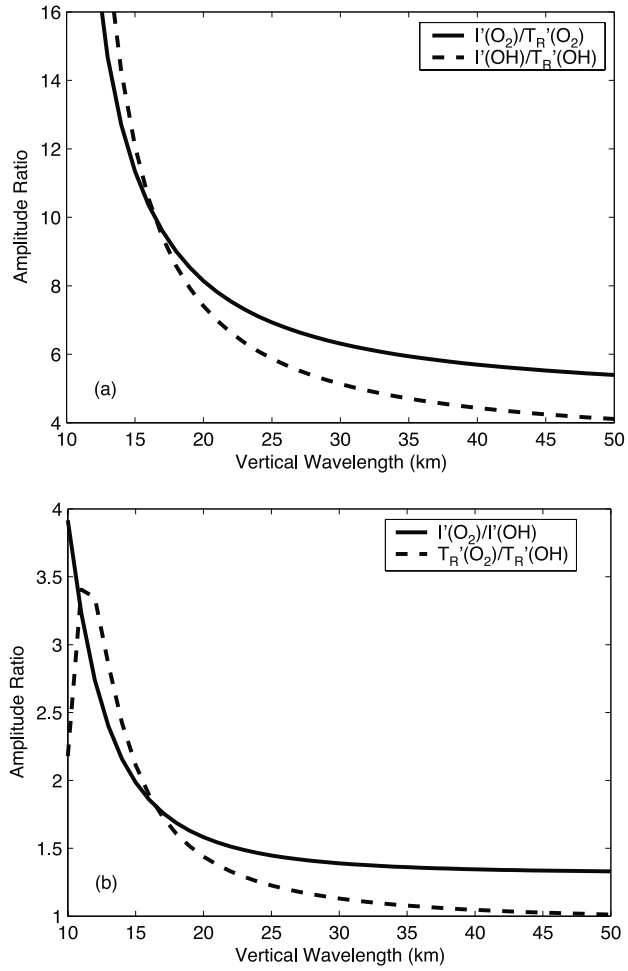

Figure 5. Ratios of relative amplitudes of (a) I'_{O_2} to T'_{R,O_2} (solid line) and I'_{OH} to $T'_{R,OH}$ (dashed line) and (b) I'_{O_2} to I'_{OH} (solid line) and T'_{R,O_2} to $T'_{R,OH}$ (dashed line), for saturated waves ($\beta = 1$).

For smaller λ_z, this cancellation effect is more pronounced and hence the larger ratios.

3.2.2. Phase

[20] As discussed in the introduction, the vertical separation of the two airglow layers results in an observed phase difference between I'_{O_2} and I'_{OH}. The measured phase difference can be used to determine the wave propagation direction unambiguously. For upward propagating waves, the phase difference would be of opposite sign to that of the downward propagating waves, and for ducted or evanescent waves, the phase difference would be zero. To characterize these phase relations, we show in Figure 6 the phase differences between I'_{O_2} and I'_{OH}, and between T'_R and I' in each layer. The phase difference between two variables A and B is defined as the phase of A minus the phase of B. A positive phase indicates that A leads B. As expected, because of the downward phase progression, I'_{O_2} always leads I'_{OH}. Similarly, T'_R always leads I' in both layers since I' peaks at a lower altitude than T'_R. The difference is smaller as λ_z becomes larger because the layer separation becomes a smaller fraction of λ_z. The smaller phase difference between T'_R and I' for O_2 with large λ_z is due to the smaller vertical separation between the centroid heights of perturbed and unperturbed volume emission profiles in the O_2 layer (2.7 km) than in the OH layer (3.1 km, see Table 1 and Figure 3).

3.3. Effects of Damping on Amplitude and Phase

[21] AGWs in the mesopause region often grow to large amplitude that cause waves to break and to dissipate. The waves observed in the OH layer are often being dissipated when they reach the O_2 layer. In previous subsection we focused on the relations between the vertical wavelength and the amplitude and phase for saturated waves ($\beta = 1$). These relations are also influenced by the damping factor β. In this subsection we show the effects of β on these relations. These results can be used in observational studies to infer the wave dissipation rate between the two airglow layers.

3.3.1. Amplitude

[22] The ratio of the relative amplitude of I'_{O_2} to I'_{OH} for various damping rate β and λ_z were calculated and shown as a contour plot in Figure 7. For undamped ($\beta = 0$) waves, the ratio varies from 2.7 to 1.8 for λ_z from 15 km to 50 km. As β increases, this ratio decreases as expected. For small λ_z (less than 15 km), the cancellation effect becomes large, and the difference in layer thickness becomes a factor in the amplitude ratio. Because the OH layer is thicker than the O_2 layer and therefore has a stronger cancellation effect, this amplitude ratio increases rapidly as λ_z decreases. This results in a high sensitivity of the amplitude ratio versus λ_z.

[23] Figure 8 shows the same relation but with the damping rate plotted against λ_z and amplitude ratio. In observation, the amplitude ratio and λ_z from these two airglow layers can be measured and then compared with this contour plot to estimate the damping factor and the wave dissipation rate. Because of the high sensitivity of β versus λ_z for $\lambda_z < 15$ km, even small uncertainties in λ_z would result in large uncertainties in β. Therefore estimating

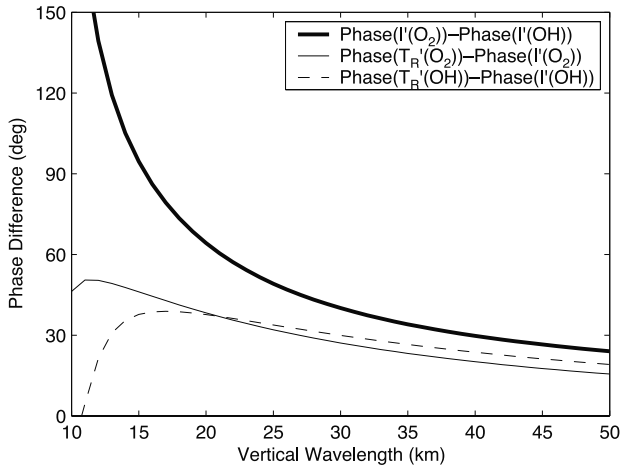

Figure 6. Phase differences between I'_{O_2} and I'_{OH} (thick solid line), T'_{R,O_2} and I'_{O_2} (thin solid line) and $T'_{R,OH}$ and I'_{OH} (dashed line) for saturated waves ($\beta = 1$). Phase difference between A and B is defined as phase of A minus phase of B. Positive phase indicates A leads B.

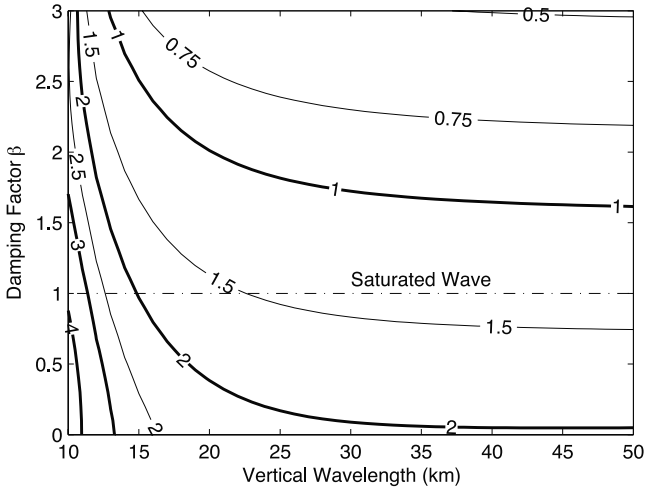

Figure 7. Contour plot of the ratio of relative amplitude of I'_{O_2} to I'_{OH} as a function of β and λ_z.

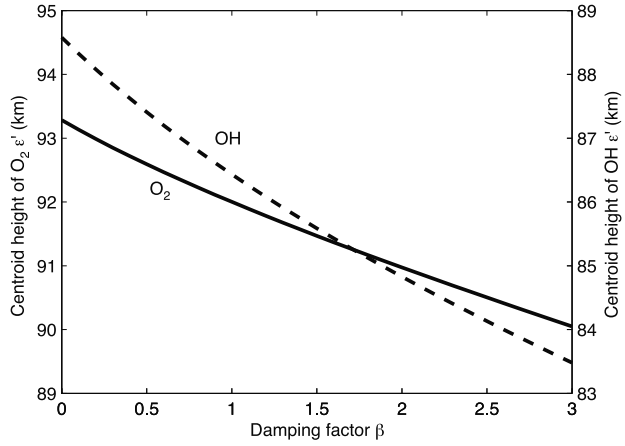

Figure 9. Centroid heights of standard deviation profiles of O_2 (solid) and OH (dashed) volume emission perturbations as functions of β for waves with λ_z = 25 km.

the dissipation rate is most applicable for large λ_z (>15 km), where β is not very sensitive to λ_z and mostly dependent on the amplitude ratio only. As an example, the observed amplitude ratio and λ_z of waves observed by *Reisin and Scheer* [1996] and E. R. Reisin (personal communication, 2002) are also plotted in Figure 8. Most waves show some degree of damping, and a large part of them are heavily damped (β > 1).

3.3.2. Phase

[24] The damping rate can also affect the phase relation. When the waves are heavily damped, their amplitudes decrease rapidly through the airglow layer, resulting in a lowered centroid height of the standard deviation profile of the volume emission perturbation. Figure 9 shows the variations of the centroid heights for O_2 and OH as functions of the damping factor β for waves with λ_z = 25 km. The centroid heights monotonically decrease as the damping increases for both O_2 and OH. The decrease is faster in OH than in O_2. For example, with β = 3, the centroid height is 90 km and 83.5 km for O_2 and OH perturbations, respectively, with a difference of 6.5 km, increased from 5.6 km when β = 1 (Table 1). As a result, the phase difference between I'_{O_2} and I'_{OH} increases as β increases.

[25] Figure 10 shows the phase differences as functions of β and λ_z. Figure 10a shows that the phase difference between I'_{O_2} and I'_{OH} indeed increases with β for reason discussed above. The difference is largest for waves with small λ_z and strong damping. Figures 10b and 10c show that the phase differences between I' and T'_R within each layers decrease as β increases. The results in Figure 10 indicate that the phase difference is strongly dependent on both λ_z and β. It is important to take into account the wave damping when estimating λ_z from measured phase difference.

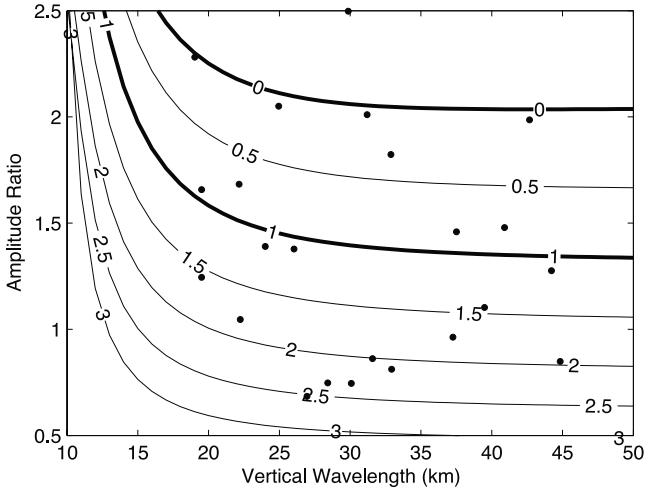

Figure 8. Contour plot of the damping rate β as a function of λ_z and amplitude ratio of I'_{O_2} to I'_{OH}. The dots are observed values based on data from *Reisin and Scheer* [1996] and E. R. Reisin (personal communication). The contours for β = 0 (freely propagating) and β = 1 (saturated) are highlighted with thick lines.

4. Summary and Discussion

[26] We have constructed a one-dimensional model to simulate the airglow perturbations in the O_2 and OH layers generated by gravity waves. The relations between the wave parameters of AGWs and the perturbations in the airglow intensity and the rotational temperature are derived. Because of the vertical separation of the O_2 and OH layers, amplitude and phase from these two airglow intensity perturbations I' and their corresponding rotational temperature perturbations T'_R are different and are functions of wave parameters. For upward propagating (downward phase progression) waves, the O_2 perturbation always leads the OH perturbation because the O_2 layer is above the OH layer. The rotational temperature perturbation T'_R leads the intensity perturbation I' in each layer because the centroid height of the standard deviation profile of perturbed volume emission is lower than that of the unperturbed volume emission profile. For downward propagating waves, these phase relations would be just the opposite. For evanescent waves, there is no phase difference among these quantities. In observation the vertical propagation directions can be

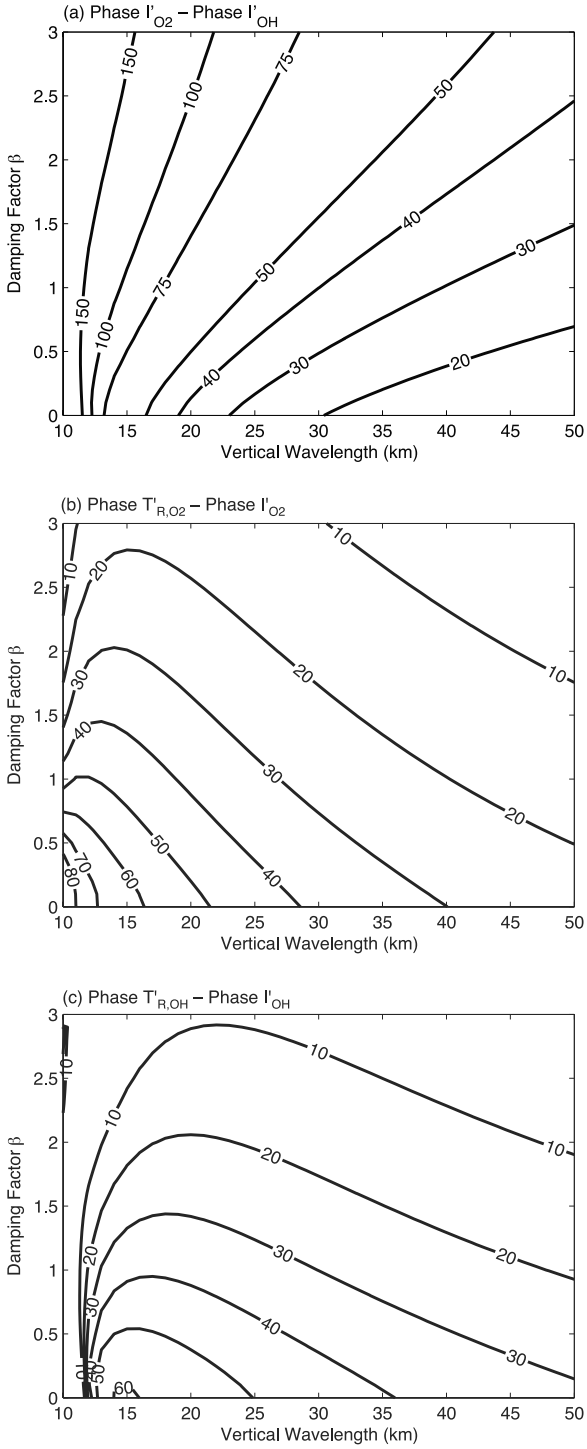

Figure 10. Contour plots of the phase differences between (a) I'_{O_2} and I'_{OH}, (b) T'_{R,O_2} and I'_{O_2} and (c) $T'_{R,OH}$ and I'_{OH}, as functions of λ_z and β. Phase difference between A and B is defined as phase of A minus phase of B. Positive phase indicates A leads B.

determined from the measured phase difference between the O_2 and OH intensity perturbations, as well as from phase difference in T'_R.

[27] Because of the finite thickness of the airglow layers, perturbations with small vertical scale have strong cancellation in the layer and therefore do not show significant amplitudes from the ground observation. The model shows that I' and T'_R are not sensitive to waves with $\lambda_z < 10$ km. The relative amplitude ratio of I'_{O_2} to I'_{OH} is related to λ_z and the damping rate β. This ratio is largest for undamped waves and decreases as the wave damping increases. As λ_z decreases and approaches the thickness of the airglow layers, the difference in cancellation effect in the two layers becomes significant. Since the OH layer is slightly thicker than the O_2 layer in the model, stronger cancellation in the OH layer causes this ratio to increase as λ_z decreases.

[28] The model also shows that the standard deviation of volume emission perturbation has a centroid height that is 2–3 km lower than that of the unperturbed volume emission profile in both O_2 and OH layers. This implies that the airglow perturbations observed from ground mainly come from an altitude that is lower than the volume emission profile. When studying gravity waves with airglow, wind measurements from other instruments such as radar or lidar are often used to derive intrinsic wave parameters. The wind that applied to this type of study should be weighted by the profile of the standard deviation, not the volume emission. The difference can be significant when there is a large wind shear. This difference in centroid heights also increases as the wave damping increases, and causes the phase difference between O_2 and OH to increase. Therefore the wave damping and the phase information are both necessary to derive correct wave parameters.

[29] In studying the AGW effects on the middle atmosphere, it is a major concern to distinguish freely propagating waves from evanescent or ducted waves. This study investigates the phase and amplitude characteristics related to freely propagating waves with various damping rate and vertical wavelengths. These relations can be used to infer wave's vertical propagation directions and dissipation rate from observed phase and amplitude in O_2 and OH layers. Evanescent waves can also be determined when there is no phase difference in the airglow perturbation from these two layers. A good example of downward propagating waves and their phase relationships is described in a measurement by *Ejiri et al.* [2001], who showed a clear packet of high frequency waves propagating downward.

[30] It is noted that the vertical flux of horizontal momentum of the wave field is approximately proportional to the product of the ratio of the vertical wavelength to the horizontal wavelength (λ_z/λ_h) and the square of the relative perturbation amplitude [*Swenson and Liu*, 1998]. The ratio λ_z/λ_h for the very high frequency waves observed in OH at Albuquerque for example [*Swenson et al.*, 2000] is 0.5–1, similar to those described by *Ejiri et al.* [2001]. It is most important to resolve the characteristics of these high frequency waves which potentially carry the majority of the momentum flux for estimating their net effect on the large scale dynamics in the upper mesosphere and lower thermosphere.

[31] It is important to note that these results are from a highly simplified model. It serves to illustrate the fundamental mechanisms of the variation of phase and amplitude due to AGWs and how they can be used to infer AGW parameters. In the real atmosphere, the vertical displacement of O_2 and OH layers can easily change the phase and amplitude relations of airglow perturbations observed from

ground. For example, in some observations, vertical wavelengths of 5–10 km have been observed, which is likely due to unusually thin OH layers that may result from coupled dynamical effects of gravity waves and tides. Recently, an O_2 profile measured from TOMEX rocket experiment showed an O_2 layer that was pushed down to below 90 km [*Hecht et al.*, 2001a]. The phase relation can also be altered by tidal variation, which is strong in middle and low latitudes, especially the diurnal tide that has a relatively short vertical wavelength. Studies of these effects are beyond the scope of this paper but are clearly important for further investigations. To better determine AGWs characteristics from airglow measurements, the vertical distribution of volume emission rates needs to be measured. Satellite are best suited for this type of observation.

[32] **Acknowledgments.** We would like to thank E. R. Reisin for kindly providing the observational data used in this study. Two reviewers' comments greatly improved this manuscript. This work was supported by NASA grants NAG 5-10072 and NAG 5-10754 and NSF grant ATM 99-08598.

References

Burrage, M. D., N. Arvin, W. R. Skinner, and P. B. Hays, Observations of the O_2 atmospheric band nightglow by the High Resolution Doppler Imager, *J. Geophys. Res.*, *99*, 15,017–15,023, 1994.

Ejiri, M. K., K. Shiokawa, T. Ogawa, T. Nakamura, R. Maekawa, T. Tsuda, and M. Kubota, Small-scale gravity waves near the mesopause observed by four all-sky airglow imagers, *J. Geophys. Res.*, *106*, 22,793–22,799, 2001.

Greer, R. G. H., E. J. Llewellyn, B. H. Solheim, and G. Witt, The excitation of $O_2(b^1\Sigma_g^+)$ in the nightglow, *Planet. Space Sci.*, *29*, 383–389, 1981.

Hecht, J. H., J. H. Clemmons, M. F. Larsen, A. Z. Liu, and R. G. Roble, First results from the photometer experiment on TOMEX, *Eos Trans. AGU*, *82*(47), F965, Fall. Meet. Suppl., 2001a.

Hecht, J. H., R. L. Walterscheid, and R. A. Vincent, Airglow observations of dynamical (wind shear-induced) instabilities over Adelaide, Australia, associated with atmospheric gravity waves, *J. Geophys. Res.*, *106*, 28,189–28,197, 2001b.

Hedin, A. E., Extension of the MSIS thermosphere model into the middle and lower atmosphere, *J. Geophys. Res.*, *96*, 1159–1172, 1991.

Hickey, M. P., G. Schubert, and R. L. Walterscheid, Gravity wave-driven fluctuations in the O_2 Atmospheric (0-1) nightglow from an extended, dissipative emission region, *J. Geophys. Res.*, *98*, 13,717–13,729, 1993.

Hickey, M. P., R. L. Walterscheid, M. J. Taylor, W. E. Ward, G. Schubert, Q. Zhou, F. Garcia, M. C. Kelly, and G. G. Shepherd, Numerical simulations of gravity waves imaged over Arecibo during the 10-day January 1993 campaign, *J. Geophys. Res.*, *102*, 11,475–11,489, 1997.

Hines, C. O., Internal atmospheric gravity waves at ionospheric heights, *Can. J. Phys.*, *38*, 1441–1481, 1960.

Krassovsky, V. I., Infrasonic variations of OH emission in the upper atmosphere, *Ann. Geophys.*, *28*, 739–746, 1972.

Makhlouf, U. B., R. H. Picard, and J. R. Winick, Photochemical-dynamical modeling of the measured response of airglow to gravity waves, *J. Geophys. Res.*, *100*, 11,289–11,311, 1995.

McDade, I. C., D. P. Murtagh, R. G. H. Greer, P. H. G. Dickinson, G. Witt, J. Stegman, E. J. Llewellyn, L. Thomas, and D. B. Jenkins, ETON 2: Quenching parameters for the proposed precursors of $O_2(b_1\Sigma_g^+)$ and $O(^1S)$ in the terrestrial nightglow, *Planet. Space Sci.*, *34*, 789–800, 1986.

Murtagh, D. P., G. Witt, J. Stegman, I. C. McDade, E. J. Llewellyn, F. Harris, and R. G. H. Greer, An assessment of proposed $O(^1S)$ and $O_2(b_1\Sigma_g^+)$ nightglow excitation parameters, *Planet. Space Sci.*, *38*, 43–53, 1990.

Reisin, E. R., and J. Scheer, Characteristics of atmospheric waves in the tidal period range derived from zenith observations of O_2 (0-1) Atmospheric and OH(6-2) airglow at lower midlatitudes, *J. Geophys. Res.*, *101*, 21,223–21,232, 1996.

Schubert, G., and R. L. Walterscheid, Wave-driven fluctuations in OH nightglow from an extended source region, *J. Geophys. Res.*, *93*, 9903–9915, 1988.

Solheim, B. H., and E. J. Llewellyn, An indirect mechanism for the production of $O(_1S)$ in the aurora, *Planet. Space Sci.*, *27*, 473–479, 1979.

Swenson, G. R., and C. S. Gardner, Analytical models for the responses of the mesospheric OH* and Na layers to atmospheric gravity waves, *J. Geophys. Res.*, *103*, 6271–6294, 1998.

Swenson, G. R., and A. Z. Liu, A model for calculating acoustic gravity wave energy and momentum flux in the mesosphere from OH airglow, *Geophys. Res. Lett.*, *25*, 477–480, 1998.

Swenson, G. R., M. J. Alexander, and R. Haque, Dispersion imposed limits on atmospheric gravity waves in the mesosphere: Observations from OH airglow, *Geophys. Res. Lett.*, *27*, 875–878, 2000.

Tarasick, D. W., and G. G. Shepherd, Effects of gravity waves on complex airglow chemistries, 1, $O_2(b^1\Sigma_g^+)$ emission, *J. Geophys. Res.*, *97*, 3185–3193, 1992a.

Tarasick, D. W., and G. G. Shepherd, Effects of gravity waves on complex airglow chemistries, 2, OH emission, *J. Geophys. Res.*, *97*, 3195–3208, 1992b.

Torr, M. R., D. G. Torr, and R. R. Laher, The O_2 atmospheric (0-0) band and related emissions at night from Spacelab 1, *J. Geophys. Res.*, *90*, 8525–8538, 1985.

Viereck, R. A., and C. S. Deehr, On the interaction between gravity waves and the OH Meinel (6-2) and the O_2 Atmospheric (0-1) bands in the polar night airglow, *J. Geophys. Res.*, *94*, 5397–5404, 1989.

Walterscheid, R. L., G. Schubert, and J. M. Straus, A dynamical-chemical model of wave-driven fluctuations in the OH nightglow, *J. Geophys. Res.*, *92*, 1241–1254, 1987.

Walterscheid, R. L., J. H. Hecht, R. A. Vincent, I. M. Reid, J. Woithe, and M. P. Hickey, Analysis and interpretation of airglow and radar observations of quasi-monochromatic gravity waves in the upper mesosphere and lower thermosphere over Adelaide, Australia (35°S, 138°E), *J. Atmos. Sol. Terr. Phys.*, *61*, 461–478, 1999.

Walterscheid, R. L., J. H. Hecht, F. T. Djuth, and C. A. Tepley, Evidence of reflection of a long-period gravity wave in observations of the nightglow over Arecibo on May 8–9, 1989, *J. Geophys. Res*, *105*, 6927–6934, 2000.

Zhang, S. P., R. N. Peterson, R. H. Wiens, and G. G. Shepherd, Gravity waves from O_2 nightglow during the AIDA '89 campaign I: Emission rate/temperature observations, *J. Atmos. Terr. Phys.*, *55*, 355–375, 1993a.

Zhang, S. P., R. H. Wiens, and G. G. Shepherd, Gravity waves from O_2 nightglow during the AIDA '89 campaign II: Numerical modeling of the emission rate/temperature ratio, η, *J. Atmos. Terr. Phys.*, *55*, 377–395, 1993b.

A. Z. Liu and G. R. Swenson, Department of Electrical and Computer Engineering, University of Illinois, 1308 West Main Street, Urbana, IL 61801, USA. (liuzr@uiuc.edu; swenson1@uiuc.edu)